JOURNAL OF AIRCRAFT
Vol. 44, No. 6, November–December 2007

Effect of Thrust-Vectoring Jets on Delta Wing Aerodynamics

Zhi-Jin Wang,* Ping Jiang,† and Ismet Gursul‡
University of Bath, Bath, BA2 7AY England, United Kingdom,

DOI: 10.2514/1.30568

The interaction of thrust-vectoring jets with leading-edge vortices over stationary delta wings and its effects on the wing aerodynamics were investigated experimentally. Two models with sweep angles of $\Lambda = 50$ and 65 deg, representing nonslender and slender wings, respectively, were tested with rectangular and circular nozzles. Force, velocity measurements, and flow visualization were performed. It was found that undervortex blowing can significantly affect the aerodynamic forces on both nonslender and slender wings. The maximum lift change occurred near the stall angle, due to the earlier reattachment of shear layer and delay of vortex breakdown. Force measurements revealed that the effect of nozzle geometry can be important, because the entrainment effect of the jet depends on it. The jet–vortex interaction, distortion of jet vortices, and merging of wing and jet vortices are more pronounced for the rectangular nozzle and have a larger influence on the delta wing aerodynamics. The effect of the jet yaw angle is small for the nonslender wing, whereas the aerodynamics of the slender wing is very sensitive to the jet yaw angle.

Nomenclature

A_{jet}	=	cross-sectional area of the nozzle exit
b	=	wingspan
C_L	=	lift coefficient
C_μ	=	jet momentum coefficient
c	=	chord length
q	=	freestream dynamic pressure
Re	=	Reynolds number
S_w	=	wing surface area
t	=	wing thickness
U_{jet}	=	jet velocity
U_∞	=	freestream velocity
u	=	velocity
X_b	=	distance from the wing apex to the leading-edge vortex breakdown location
y_{jet}	=	spanwise location of the jet
α	=	angle of attack
β	=	jet pitch angle
γ	=	jet yaw angle
ΔC_L	=	change in C_L
ΔX_b	=	change in X_b
Λ	=	leading-edge sweep angle
ν	=	fluid kinematic viscosity
ρ	=	air density
ω_x	=	streamwise vorticity

I. Introduction

HIGHLY swept wings, often referred to as delta wings, have certain advantages and are used in various applications. For example, at high angles of attack, delta wings can generate higher lift than high-aspect ratio wings, with better aircraft stability and control characteristics [1–3]. For this reason, delta wings are preferred for highly maneuverable fighter aircraft configurations. Current and future highly maneuverable unmanned combat air vehicle (UCAV) concepts are often blended delta wing–body configurations [4,5] for the same reason. It was, however, recognized recently that serious stability and control issues exist for these configurations because of the absence of conventional aerodynamic control surfaces (i.e., the fin and tailplane [5]). Tailless designs provide a number of performance and signature benefits, but to be successful, there is a need to explore and understand alternative methods of providing sufficient levels of stability and control.

One method widely anticipated for use on future UCAV configurations with tailless design is the thrust-vectoring control, as sketched in Fig. 1. With the requirement of high maneuverability for future unmanned air vehicles, interaction of vortex flows with thrust-vectoring jets becomes important. This aerodynamics–propulsion interaction may affect the properties of the leading-edge vortices and, consequently, aerodynamic forces and moments on the wing [4,5]. Also, unsteady vortex flows over stationary and maneuvering delta wings are likely to be affected by this vortex–jet interaction [6].

At high angle of attack, the leading-edge vortices undergo a sudden expansion known as vortex breakdown [7,8]. Vortex breakdown has adverse effects on wing performance (i.e., a decrease in lift for slender wings). Several investigators have examined the effects of trailing-edge jets on the vortical flow and vortex breakdown over delta wings [9–13]. These studies demonstrated that the trailing-edge jet could delay the leading-edge vortex breakdown significantly: up to 50% of the wing chord. These investigations also demonstrated that strong asymmetric breakdown of the leading-edge vortices can be induced by arranging the vectored trailing-edge jet in an asymmetric configuration. The effects of intermittent trailing-edge blowing on the leading-edge vortex breakdown on a dynamically pitching wing have also been studied [11]. It was shown that the blowing effect persists throughout the entire pitching cycle, due to the phase lag of vortex breakdown relative to the pitching motion of the wing.

These previous studies have greatly improved our understanding of the effect of the trailing-edge jets on delta wing vortical flows. However, many of the aerodynamic issues associated with the thrust vectoring remain to be explored. For example, force measurements that quantify the effect of thrust-vectoring jets on wing aerodynamics are absent from the literature. One of the main objectives of this study is to understand the effect of trailing-edge jets on aerodynamic forces.

Received 21 February 2007; revision received 4 May 2007; accepted for publication 4 May 2007.

*Research Councils United Kingdom Academic Fellow, Department of Mechanical Engineering.
†Graduate Student, Department of Mechanical Engineering.
‡Professor, Department of Mechanical Engineering. Associate Fellow AIAA.

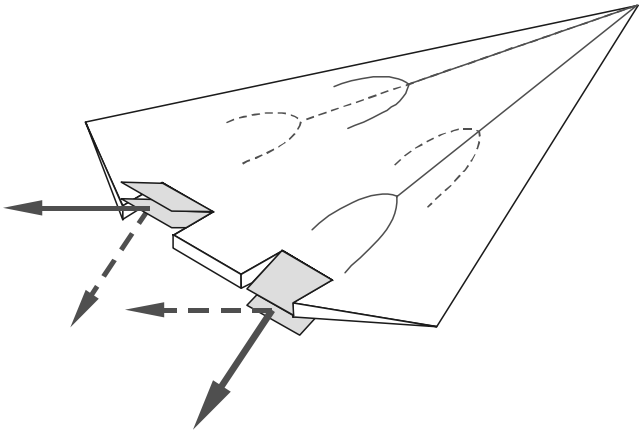

Fig. 1 Schematic of thrust-vectoring jets and leading-edge vortices.

A second objective is to understand the effect of the wing sweep angle. Important differences exist between the aerodynamics of slender and nonslender wings with regard to the structure of vortical flows, vortex breakdown, and reattachment [14]. One of the distinct features of nonslender wings is the location of the primary attachment zone outboard of the symmetry plane. Reattachment location correlates with the wing stall process and increased buffeting. The effect of trailing-edge jets for nonslender wings is largely unexplored. The two exceptions are [15], which studied a wing with $\Lambda = 50$ deg, and [16], which studied the wing near-surface flow patterns for a wing with $\Lambda = 35$ deg.

Another aspect that remains to be studied is the effect of nozzle geometry, which affects the entrainment process and the interaction between the jet and the wing vortices [17]. As the jet exhausts into crossflow, a counter-rotating vortex pair is generated (see, for example, [18,19]). One of the objectives of this paper is to understand the scale of these effects and how they affect the wing aerodynamic performance.

This paper presents an experimental investigation of the interaction of statically pitched trailing-edge jets with leading-edge vortices over stationary delta wings and its effects on the wing aerodynamics. Wind-tunnel and water-tunnel experiments were performed to simulate thrust vectoring and quantify the aerodynamic effects by means of force measurements, flow visualization, and velocity measurements. The effects of the jet location, pitch angle, yaw angle, nozzle geometry, and wing sweep angle on aerodynamic forces and vortex–jet interaction were investigated.

II. Experimental Methods

A. Aerodynamic Force Measurements

Force measurements were conducted in the high-speed working section, with a cross section of 2.13×1.52 m, of a closed-circuit wind tunnel. Two models with sweep angles of $\Lambda = 50$ and 65 deg, representing nonslender and slender delta wings, respectively, were tested. Both models had a chord length of $c = 310$ mm and a thickness-to-chord ratio of $t/c = 4.1\%$. Both models had a 45-deg bevel on the leading edges, thus producing a sharp leading edge and a square trailing edge. Models were mounted on the high-incidence rig through a six-component strain-gauged internal balance. The balance has dimensions of $138 \times 19 \times 24$ mm. Models were mounted in the tunnel using a streamlined strut projecting from the wing's lower surface. The strut was attached on the high-incidence rig through the internal force balance. With this arrangement, any unwanted interference with the leading-edge vortices is minimized. Furthermore, maximum blockage for the wind-tunnel models was approximately 1.6% at $\alpha = 40$ deg. No correction was made on the force data due to the blockage effect.

The experimental arrangement is shown schematically in Fig. 2. Only one jet is used, which simulates conditions when a rolling moment is desired in flight. A statically pitched and yawed jet system was fitted at the trailing edge of the wing models. To study the

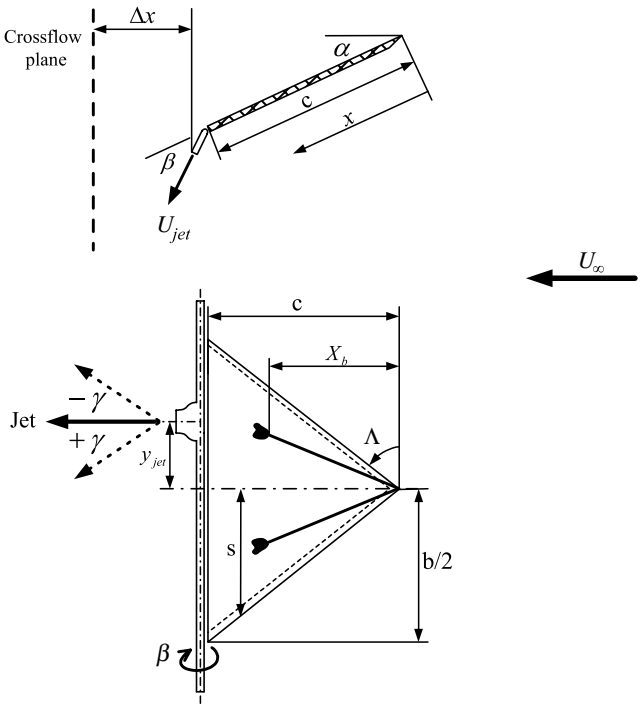

Fig. 2 Experimental arrangement.

blowing effect at different spanwise positions, nozzles were designed to move parallel to the wing's trailing edge. The jet fluid is pumped in a pipe and then fed into the nozzle. This design allows easy change of the jet pitch angle β by rotating the pipe-nozzle assembly for both static and dynamic variations. The feed pipe has an outer diameter of 12.7 mm, which is the same as the wing thickness. The pipe was placed in line with the wing's trailing edge; thus, changing the jet pitch angle by rotating the pipe did not affect the flow structure. During the experiments, there is no contact between the jet system and the wing, thus ensuring that any changes in the force measurements are solely from the blowing effects. The gap between the pipe feeding the nozzle and the wing was $0.02c$. The effect of the gap on the aerodynamic forces was investigated and it was found that no noticeable effect existed for up to $0.08c$. For all experiments reported in this paper, the gap was fixed at $0.02c$. To study the effect of the jet geometry, both rectangular (6×36 mm, with an aspect ratio of 6) and circular ($d = 10$ mm) nozzles were tested. For both rectangular and circular nozzles, the uppermost boundary is in line with the wing's trailing edge.

Experiments were conducted at a constant freestream velocity of $U_\infty = 15$ m/s, giving Reynolds numbers ($Re = U_\infty c/\nu$, where U_∞ is the freestream velocity and ν is the fluid kinematic viscosity) of $Re = 3.1 \times 10^5$ for both wings. For the purpose of comparison, experiments were carried out at the same jet momentum coefficient ($C_\mu = \rho U_{\text{jet}}^2 A_{\text{jet}} / \frac{1}{2}\rho U_\infty^2 S_w$, where A_{jet} and S_w denote the cross-sectional area of the nozzle exit and surface area of the wing) of 0.24 for both wings. The momentum coefficient has been previously used in [9–13]. The values of the momentum coefficient used in the experiments are realistic and also consistent with the range used by previous investigators. Force measurements were carried out for wing incidences of $\alpha = 3$–40 deg. A total of five values of the jet pitch angle were tested (i.e., $\beta = 0$, 10, 20, 30, and 40 deg). The jet yaw angle effects at $\gamma = -30$ deg (outboard) and 30 deg (inboard) were also investigated (see Fig. 2). For these values of yaw angles, special nozzles that fit into the feeding pipe were designed.

Signals from the force balance were simultaneously digitized using a 12-bit A/D board and a personal computer at a sampling frequency of 1 kHz per channel. The duration of each record was about 10 s. This was verified to be sufficiently long for the root mean square (rms) value of the measured signals to reach a steady value (variation of less than 1.0%). The measured forces were then normalized by qS_w (moments by $qS_w c$), where $q = \frac{1}{2}\rho U_\infty^2$ is the

freestream dynamic pressure. The measurement uncertainty for the lift coefficient is estimated to be 2%.

B. Flow Visualization

Flow visualization was conducted in a water tunnel. The tunnel is an Eidetics Model 1520 free-surface tunnel with a 0.381×0.508 m working section and can achieve speeds up to 0.45 m/s through a closed-circuit continuous-flow system. The tunnel has four viewing windows, three surrounding the test section and one downstream, allowing axial viewing. The height of the test section above the floor allows flow visualization from below as well as from the sides.

The water-tunnel experimental arrangement was scaled down from that of the wind-tunnel tests (Sec. II.A). Both wing models ($\Lambda = 50$ and 65 deg) had a chord length of $c = 100$ mm and a thickness-to-chord ratio of $t/c = 4.1\%$. Both models had a 45-deg bevel on the leading edges and a square trailing edge. The wings were mounted upside down on a streamlined sting projecting from the rear of the model. The changes of incidence α were achieved by swinging the whole experimental system, including the wing and jet system, backward or forward.

To visualize the leading-edge vortex trajectories, food-coloring dye diluted 1:4 with water was released at the wing apex. A digital video camera recorder was used to record the leading-edge vortex trajectories at a rate of 25 frames per second and a resolution of 570,000 pixels. The captured images were interfaced to a desktop computer via the commercial software package Pinnacle Studio DV, enabling real-time viewing of the wing flow visualization and the capture of camera images and video recordings. The flow visualization tests were carried out at a freestream velocity of $U_\infty = 0.3$ m/s, giving Reynolds numbers of $Re = 3.0 \times 10^4$. Four values of the jet momentum coefficient were tested: $C_\mu = 0$, 0.24, 0.43, and 1. The recording duration was typically 20 s. Experimental uncertainty in locating the vortex breakdown position was estimated to be approximately 2% of the chord length.

Flow visualization in crossflow planes (normal to the freestream direction) above the wing models and in the near-wake was performed using fluorescent dye, which was released from slots (of 0.5-mm thickness) near the leading edges, and therefore "marked" the vorticity shed with separation. Different colors of fluorescent dye were used to visualize the leading-edge vortex, jet, and their interaction, although the pictures presented in this paper are in grayscale. A 12-W argon-ion laser was used in these experiments. Light is transmitted via a fiber optic cable to the optical head, and a combination of various lenses is used to generate a light sheet.

C. PIV Measurements

To obtain quantitative information of the blowing effect on the flowfield, particle image velocimetry (PIV) measurements were carried out in the water tunnel. The tunnel and other experimental conditions were the same as those used for flow visualization tests. The model surface was painted black to minimize reflection noises. The flow was seeded with commercially available hollow glass particles with a mean diameter of 4 μm. The PIV camera was placed near the downstream viewing window to measure the velocity field in a crossflow plane. In additional experiments, the camera was placed underneath the tunnel's working section and the light sheet was placed parallel and close to the wing surface (1 mm) to reveal the near-surface flow pattern.

Illumination was provided by the laser sheets (with a thickness of 2 mm) generated by a combination of cylindrical and spherical lenses from a pair of pulsed mini Nd:YAG lasers with a maximum energy of 120 mJ per pulse. The digital particle images from the PIV measurements were taken using an 8-bit CCD camera with a resolution of 4.2 million pixels. The commercial software package Insight 6.0 and a Hart cross-correlation algorithm were used to analyze the images. In image processing, an interrogation window size of 32×32 pixels was used, thus producing velocity vectors for further processing. The effective grid size was varied from 2.4 mm in crossflow planes to 3.0 mm in a plane near the wing surface. The estimated uncertainty for velocity measurements is 2%. For each case, sequences of 100 instantaneous frames were taken at a frame rate of 3.75 Hz and the time-averaged velocity and vorticity fields were calculated.

III. Results

A. Nonslender Wing

When there was no trailing-edge blowing ($C_\mu = 0$), the measurement of lift coefficient (not shown here) demonstrated that the maximum C_L was about 1.1 for the nonslender wing ($\Lambda = 50$ deg), which occurred near the stall angle of $\alpha = 20$ deg. These results are in agreement with those reported in the literature [1,20]. Figure 3 presents the changes in C_L for the nonslender wing ($\Lambda = 50$ deg) under the effect of trailing-edge blowing of $C_\mu = 0.24$ with a rectangular nozzle, where $\Delta C_L = (C_L)_{\text{jet on}} - (C_L)_{\text{jet off}}$. Because there is no contact between the jet system and the wing, the measured ΔC_L is due to the jet/vortex interaction only. Two observations can be made from Fig. 3. First, the blowing effect on C_L depends on the jet spanwise position $y_{\text{jet}}/\frac{1}{2}b$, where y_{jet} is the distance between the nozzle and the model centerline, and b is the wingspan (see Fig. 2). When the jet was located at the center of the wing ($y_{\text{jet}}/\frac{1}{2}b = 0$), the blowing effect on C_L was relatively small. It is noted that ΔC_L appears to decrease slightly, which is more evident near the stall angle of $\alpha = 20$ deg. In contrast, when the jet was located at $y_{\text{jet}}/\frac{1}{2}b = 0.6$, which is the approximate position of the leading-edge vortex axis, the blowing resulted in much greater changes in C_L. The ΔC_L appears to increase with increasing wing incidence α. The ΔC_L reaches its maximum values (i.e., $\Delta C_{L,\max} \approx 0.15$) near the wing stall angle of $\alpha = 20$ deg. Second, for undervortex blowing ($y_{\text{jet}}/\frac{1}{2}b = 0.6$), the variations of ΔC_L associated with the jet pitch angle ($\beta = 0$ and 30 deg) are similar to each other. This observation suggests that the effect of the jet pitch angle on delta wing aerodynamics was relatively small in this case. Variation of pitching moment (not shown here) is very similar to that of the lift coefficient and will not be discussed here.

These force measurements can be interpreted in relation to the crossflow visualization pictures shown in Fig. 4. (The wing is mounted upside down in the water tunnel. In this figure, the picture is flipped to represent it right side up.) The jet is located at $y_{\text{jet}}/(b/2) = -0.6$ (left-hand side in the picture) and the light sheet is located at $x/c = 0.8$. It is seen that for incidences $\alpha = 10$ and 15 deg, the effect of the trailing-edge blowing is small, although the reattachment location is more outboard for the left vortex. (The vertical dashed line shows the wing centerline.) For the stall angle of $\alpha = 20$ deg, the left vortex appears somewhat smaller and reattaches much earlier. Note that the right vortex reattaches just near the wing centerline. For the largest angle of attack ($\alpha = 25$ deg, poststall region), separated flows on both sides appear to merge. The vertical extent of the left vortex is smaller, due to the jet blowing.

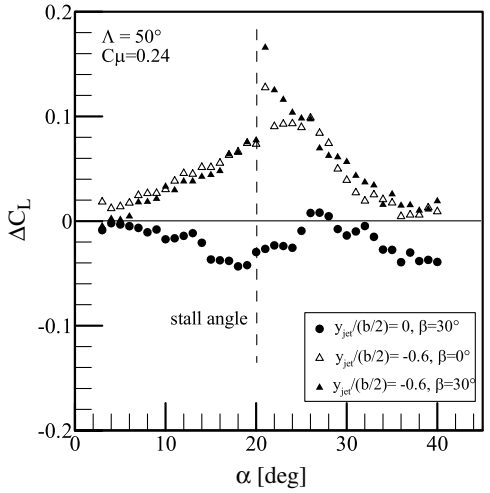

Fig. 3 Changes in lift coefficient for the nonslender wing ($\Lambda = 50$ deg) with trailing-edge blowing with a rectangular nozzle.

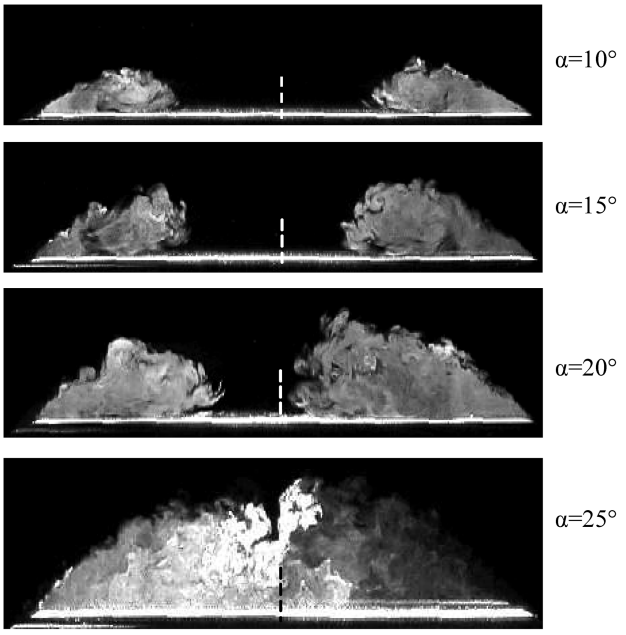

Fig. 4 Laser-fluorescence flow visualization pictures in a crossflow plane for a nonslender wing ($\Lambda = 50$ deg) with $\beta = 30$ deg, $C_\mu = 0.43$, and $y_{\text{jet}}/(b/2) = -0.6$; a laser sheet was placed at $x/c = 0.8$.

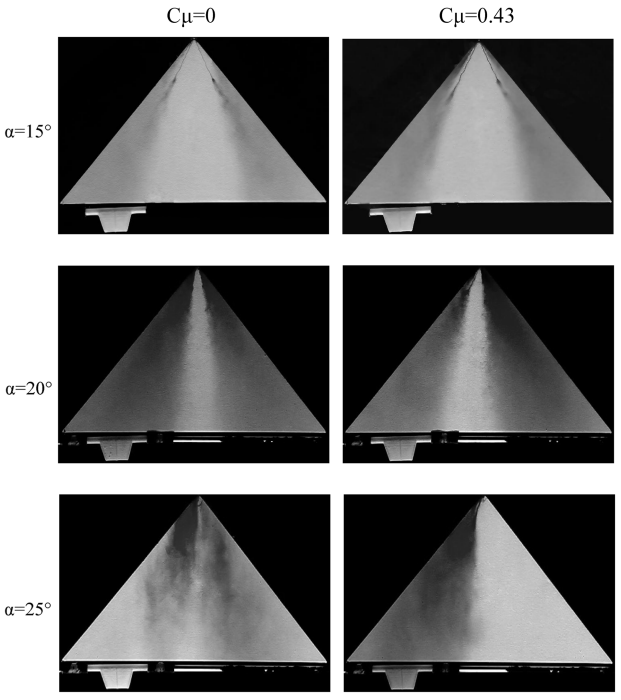

Fig. 5 Food-coloring-dye flow visualization for a nonslender wing ($\Lambda = 50$ deg) with $y_{\text{jet}}/(b/2) = -0.6$ and $\beta = 0$.

For a different value of pitch angle β, food-coloring-dye visualization pictures are shown in Fig. 5. It is seen that in the prestall region ($\alpha = 15$ deg), the change in the breakdown location with blowing is small. For $\alpha = 20$ deg (stall angle), when there is no blowing ($C_\mu = 0$), vortex breakdown occurred at the wing apex. With the trailing-edge blowing on the left side and under the vortex [$y_{\text{jet}}/(b/2) = -0.6$], however, breakdown of the leading-edge vortex on the jet side is delayed. This observation is consistent with the observed lift enhancement with undervortex blowing (see Fig. 3). Even for $\alpha = 25$ deg in the poststall region, the flow appears to be more organized with blowing. This is again consistent with the increased lift shown in Fig. 3 in the poststall region.

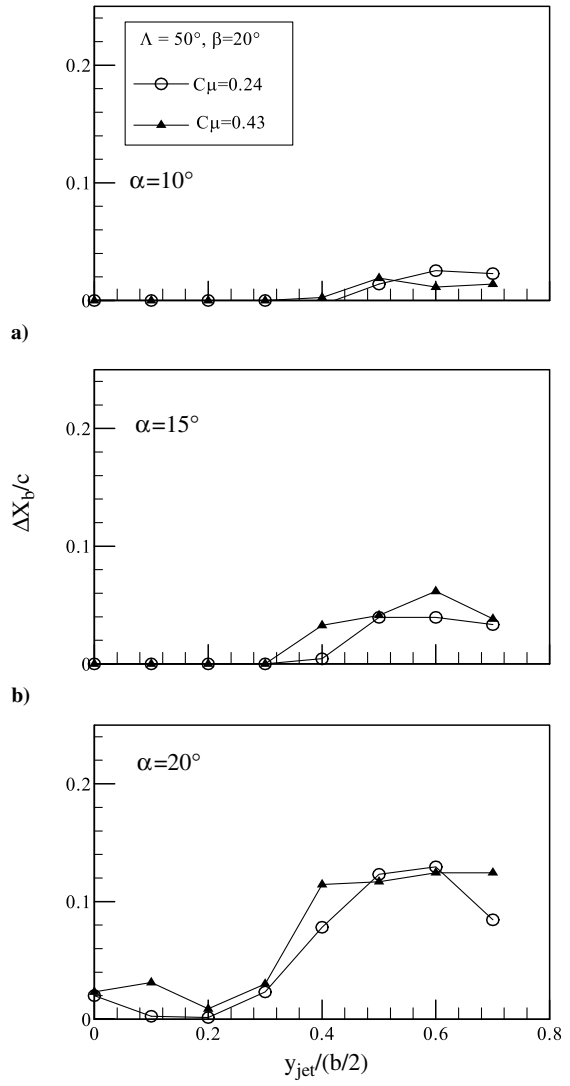

Fig. 6 Variation of the delay of the vortex breakdown location as a function of the spanwise location of the jet with $\beta = 20$ deg and a rectangular nozzle.

Figure 6 presents the variation of changes in vortex breakdown location over the nonslender wing ($\Lambda = 50$ deg) as a function of the jet location under the effect of rectangular jet blowing for various incidences; $\Delta X_b/c = (X_b/c)_{\text{jet on}} - (X_b/c)_{\text{jet off}}$, where X_b, identified from flow visualization images, is the distance from the wing apex to the vortex breakdown location (see Fig. 2). Several observations can be made based on Fig. 6. First, for all incidences tested, the maximum $\Delta X_b/c$ occurs at or near $y_{\text{jet}}/\frac{1}{2}b = 0.6$ (the approximate position of the leading-edge vortex in the spanwise direction [20]), thus suggesting a much larger effect of undervortex blowing on the vortex characteristics over the wings. Second, for undervortex blowing, the blowing effect appears to increase with increasing wing incidence α. The maximum $\Delta X_b/c$ is about 0.02 at $\alpha = 10$ deg (Fig. 6a). This value increases to $\Delta X_b/c \approx 0.05$ at $\alpha = 15$ deg (Fig. 6b) and increases further to $\Delta X_b/c \approx 0.13$ for $\alpha = 20$ deg (Fig. 6c), which corresponds to the stall angle. Third, the blowing effect at or near the wing centerline is relatively small, especially for small wing incidences. The blowing has no obvious effect on the vortex breakdown location until the jet spanwise positions $y_{\text{jet}}/(\frac{1}{2}b) \geq 0.5, 0.4$, and 0.3, corresponding to $\alpha = 10$, 15, and 20 deg, respectively. Fourth, no significant differences in the variations of $\Delta X_b/c$ were observed for $C_\mu = 0.24$ and 0.43, suggesting that there is a saturation effect with respect to the momentum coefficient.

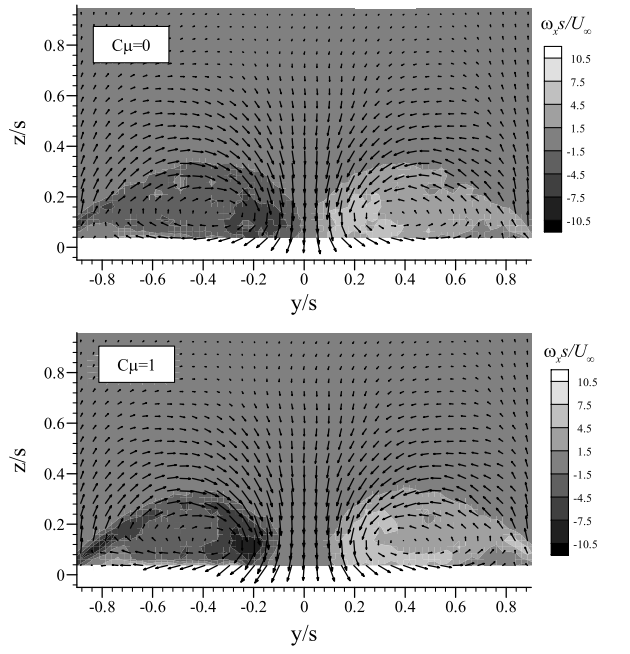

Fig. 7 Time-averaged crossflow vorticity field at $x/c = 0.8$ for the nonslender wing with $\Lambda = 50\,\text{deg}$, $\alpha = 20\,\text{deg}$, $\beta = 30\,\text{deg}$, $y_{\text{jet}}/(b/2) = -0.6$, and a rectangular nozzle.

The effects of undervortex blowing on vortex characteristics were further studied with PIV measurements. Figure 7 presents the time-averaged vorticity field measured in a crossflow plane at $x/c = 0.8$ for the nonslender wing at $\alpha = 20\,\text{deg}$ with a rectangular nozzle at $y_{\text{jet}}/(b/2) = -0.6$ and $\beta = 30\,\text{deg}$. When there is no blowing ($C_\mu = 0$), the leading-edge vortex pair is fairly symmetric about the wing centerline. Furthermore, the magnitude of $\omega_x s/U_\infty$ values is also symmetrically distributed (i.e., with a maximum $\omega_x s/U_\infty$ of about ± 6.0 for both the left and right sides). When there is undervortex blowing [$y_{\text{jet}}/(\frac{1}{2}b) = -0.6$] of $C_\mu = 1$, the maximum magnitude of $\omega_x s/U_\infty$ (≈ 12) on the jet side is higher than that on the other side and also higher than those associated with $C_\mu = 0$, apparently due to the delay of vortex breakdown. In addition, the separation distance between the leading-edge vortex pair increased. This observation suggests an earlier reattachment of the leading-edge vortex on the jet side.

The effects of trailing-edge jets on wing flow characteristics were further clarified by PIV measurements near the wing surface. Figure 8 shows the magnitude of time-averaged velocity u/U_∞ and streamline pattern near the wing surface at $\alpha = 20\,\text{deg}$. At $C_\mu = 0$ (Fig. 8a), the flow pattern is fairly symmetric about the wing centerline. Furthermore, closed spiraling streamline patterns corresponding to two nodes can be observed on both sides near the wing apex. Note that the leading-edge vortex breakdown occurred near the wing apex in this case (see Fig. 5). When there is undervortex jet blowing of $C_\mu = 0.24$, however, it can be seen that the reattachment occurs earlier on the jet (left) side. As a result, the closed spiraling streamline pattern near the wing apex persists only at the right side (Fig. 8b), though its scale is much smaller than that associated with $C_\mu = 0$ (Fig. 8a). These observations are consistent with the flow visualization results (Figs. 4 and 5). In addition, the flowfield appears asymmetric about $y = 0$ for $C_\mu = 0.24$ (Fig. 8b). The maximum u/U_∞ region appears to be shifting away from the wing centerline toward the jet (left) side, which is more evident for higher-momentum coefficients [i.e., $C_\mu = 0.43$ (Fig. 8c) and $C_\mu = 1.0$ (Fig. 8d)]. It is seen in Fig. 8 that the flow pattern near the stall for $C_\mu = 0$ exhibits a single reattachment near the wing symmetry plane, whereas two separate reattachment lines can be identified for jet blowing.

B. Slender Wing

Figure 9 presents the changes in C_L under the effect of trailing-edge blowing with the rectangular nozzle for the slender wing ($\Lambda = 65\,\text{deg}$). Note that the stall angle shifts to $\alpha = 32\,\text{deg}$ and the maximum C_L is about 1.5 (not shown here) for no blowing. These results are in agreement with those reported in the literature [2,3]. It is observed that the centerline blowing causes C_L to decrease up to about 0.07 for $C_\mu = 0.43$, whereas the undervortex blowing tends to increase C_L, which persists even after the slender-wing stall angle of

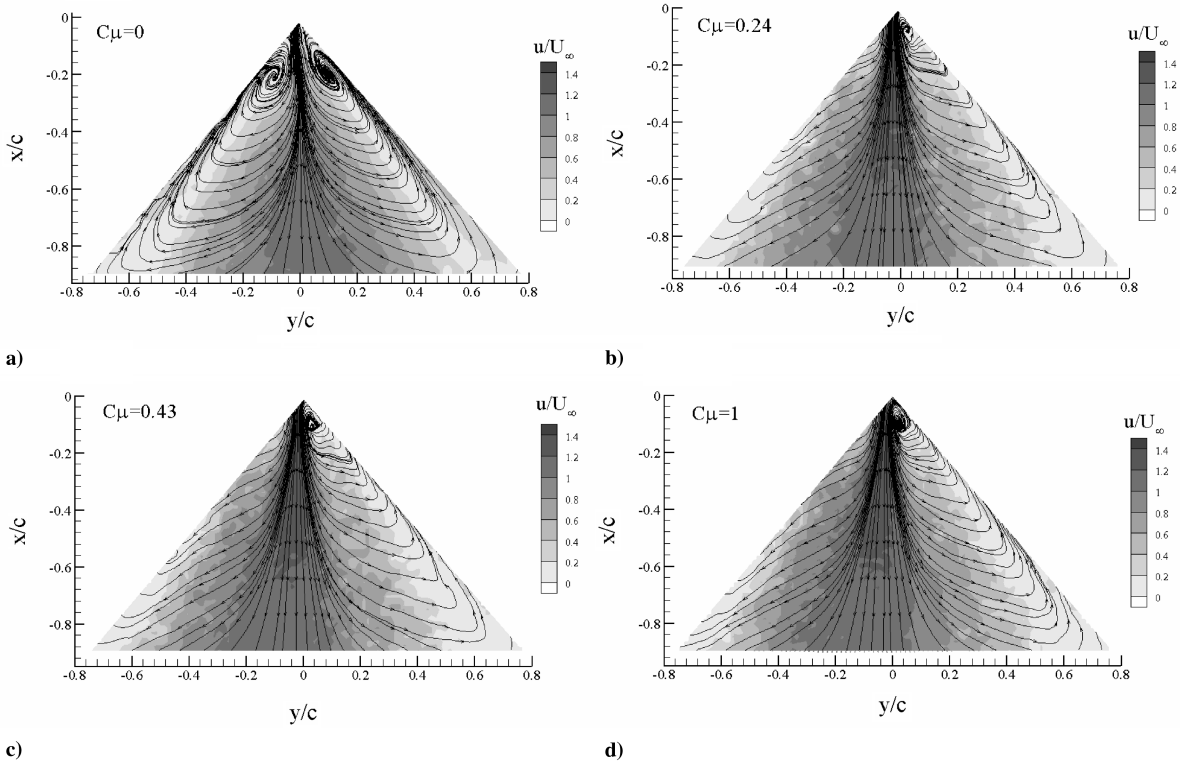

Fig. 8 Magnitude of time-averaged velocity and streamline pattern near the wing surface with $\Lambda = 50\,\text{deg}$, $\alpha = 20\,\text{deg}$, $\beta = 30\,\text{deg}$, $y_{\text{jet}}/(b/2) = -0.6$, and a rectangular nozzle.

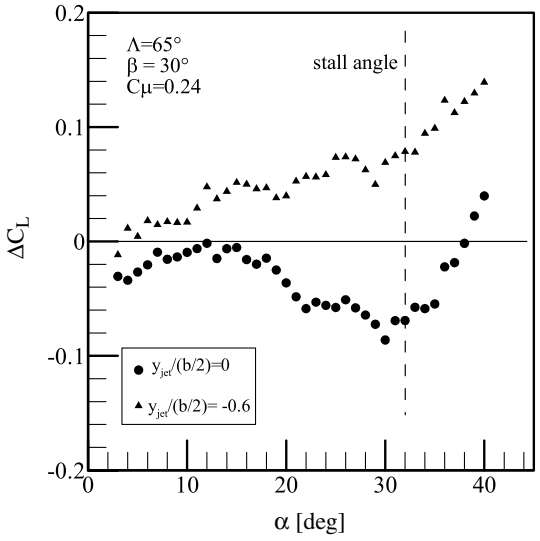

Fig. 9 Changes in C_L under the effect of blowing with a rectangular nozzle for a slender wing.

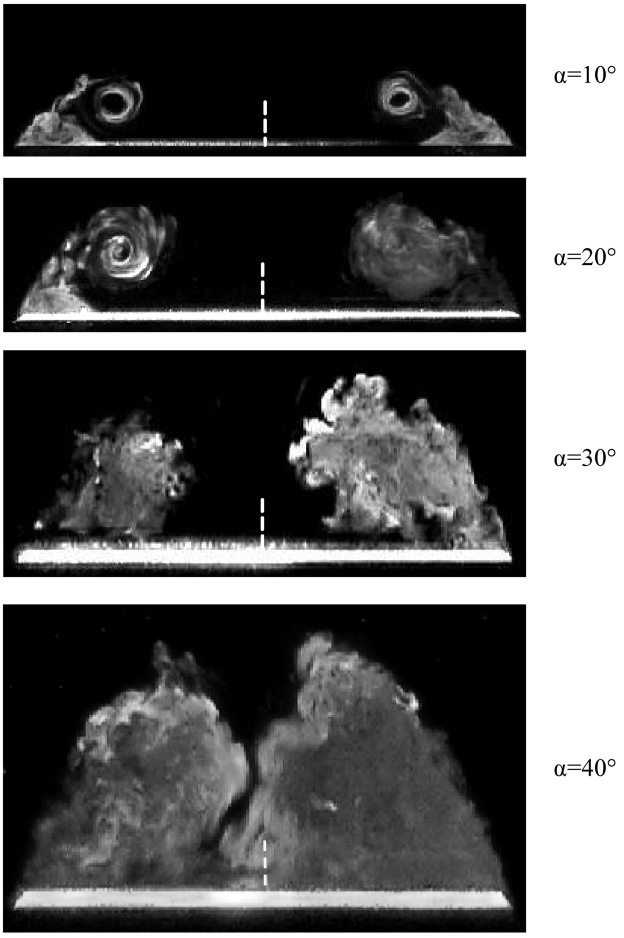

Fig. 10 Laser-fluorescence flow visualization pictures for a slender wing ($\Lambda = 65$ deg) with $\beta = 30$ deg and $C_\mu = 0.43$; a laser sheet was placed at $x/c = 0.8$.

$\alpha = 32$ deg. Comparison with the case of the nonslender wing (see Fig. 3) indicates that the effect of centerline blowing near the stall angle is relatively larger for the slender wing. This is reasonable, because the relative span of the slender wing is smaller.

The force measurements shown in Fig. 9 can be interpreted in relation to the crossflow visualization pictures shown in Fig. 10. The jet is located at $y_{\text{jet}}/(b/2) = -0.6$ (left-hand side in the picture) and the light sheet is located at $x/c = 0.8$. It is seen that for the smallest incidence ($\alpha = 10$ deg), the effect of blowing is small. In this picture, the dark region in the vortex core suggests the absence of vortex breakdown. For $\alpha = 20$ deg, the blowing delays vortex breakdown on the jet side (with the dark region in the core), whereas the other side exhibits a broken down vortex at that station. Again, the largest effects appear at $\alpha = 30$ deg, which is near the stall angle. The vortex on the jet side appears to be smaller in size for large angles of attack.

The overall effect of blowing is best illustrated in Fig. 11 as a function of incidence. Largest changes in the location of breakdown occur on the jet side near the stall angle of $\alpha = 32$ deg, and even at the poststall incidences such as $\alpha = 40$ deg. The other side shows a small movement of breakdown upstream, because the vortex on the jet side is delayed as a result of blowing. Figure 12 shows the variation of the delay of the vortex breakdown location as a function of the jet pitch angle for $y_{\text{jet}}/(b/2) = -0.6$ at various angles of attack. It is seen that the effect of the jet pitch angle is generally small. With increasing incidence, the delay of breakdown increases up to $\alpha = 35$ deg (which is slightly larger than the stall angle) and then decreases for $\alpha = 40$ deg. The largest delays achieved for this slender wing ($\Lambda = 65$ deg) are slightly larger than those for the nonslender wing ($\Lambda = 50$ deg).

It is interesting to examine the effectiveness of a trailing-edge jet as a function of the wing sweep angle, because blowing at the trailing-edge modifies the external pressure gradient and delays vortex breakdown. Figure 13 shows the optimum effectiveness values [defined as $(\Delta X_b/c)/C_\mu$], collected from various studies reported in [9–13,15] and from the present study, as a function of the wing sweep angle. It appears that it becomes more difficult to delay vortex breakdown with decreasing sweep angle. This is likely to be due to the fact that the external pressure gradient is more adverse for nonslender wings than for slender wings; as a result, the effectiveness of breakdown control is much lower. Even though the delay of breakdown is more difficult for nonslender wings, the effect of trailing-edge jets on the reattachment of flow is substantial, as shown near the stall angle (see Figs. 5 and 8).

C. Effect of Nozzle Geometry

In this section, the effects of nozzle geometry on lift force and jet/vortex interaction details are discussed. Figure 14 presents the changes in C_L for the nonslender wing with trailing-edge jet blowing ($C_\mu = 0.24$) and circular nozzle. It is seen that the ΔC_L exhibits similar trends to those of jet blowing with the rectangular nozzle (see Fig. 3). The effect of centerline blowing is small, and there is lift enhancement, which reaches its maximum values near the wing stall angle, for undervortex blowing. However, the magnitude of C_L changes is smaller for the circular nozzle. With undervortex blowing at $y_{\text{jet}}/(b/2) = -0.6$, the maximum ΔC_L associated with the circular nozzle is about 0.075, considerably smaller than that of the rectangular nozzle ($\Delta C_{L,\max} \approx 0.15$; see Fig. 3).

To understand the differences between the effects of circular and rectangular nozzles on ΔC_L, PIV measurements of the time-averaged vorticity field in a crossflow plane in the near wake (at 25% chord from the nozzle exit) for the nonslender wing were carried out. In addition, to better understand the effect of vortex, similar measurements were performed without the wing (and vortex) and compared with the wing (and vortex) case. Figure 15 compares the results for the circular nozzle (left column) and rectangular nozzle (right column), as well as without the wing (Figs. 15a and 15b) and with the wing (Figs. 15c and 15d). It is seen that both nozzles produce a pair of counter-rotating vortices as the jets exhaust into the crossflow when there is no vortex (Figs. 15a and 15b), and the distance between the pair of vortices is larger for the rectangular nozzle, as expected. Figure 15c shows that when there is vortical flow due to the wing at $\alpha = 20$ deg, the jet vortex with the counterclockwise vorticity is distorted under the effect of the induced velocity of the wing vortical flow (the wing vortex is not very concentrated at the stall incidence and exhibits weak vorticity). The interaction and distortion appear to be stronger for the

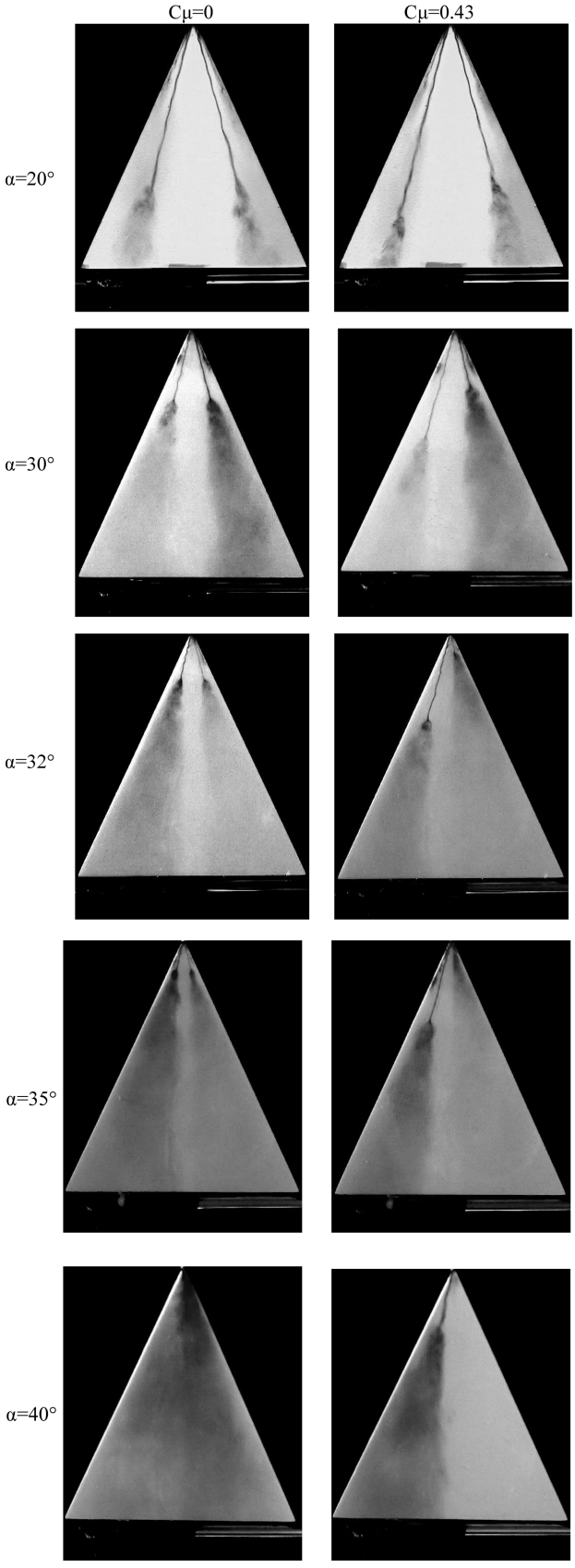

Fig. 11 Food-coloring-dye flow visualization for a slender wing ($\Lambda = 65\,\mathrm{deg}$) with $y_{\mathrm{jet}}/(b/2) = -0.5$ and $\beta = 0\,\mathrm{deg}$.

rectangular nozzle (Fig. 15d). The jet vortex with the counterclockwise vorticity seems to be split into two, and a small secondary vortex is visible. The jet vortex with clockwise vorticity appears to be much weaker as a result of this vortex–jet interaction. It is interesting

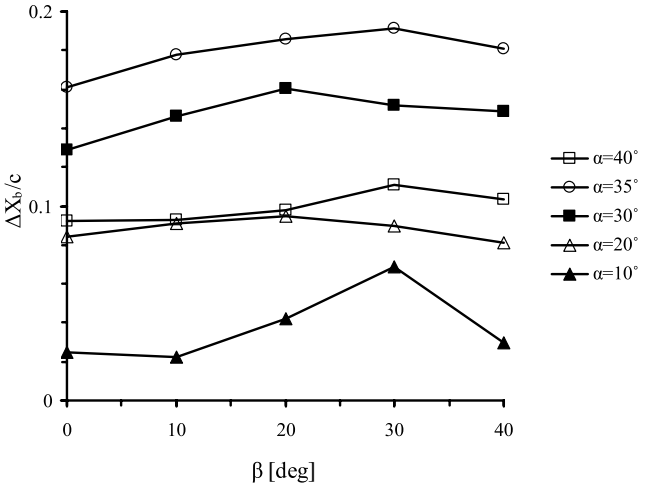

Fig. 12 Variation of the delay of the vortex breakdown location as a function of the jet pitch angle with $\Lambda = 65\,\mathrm{deg}$, $C_\mu = 0.43$, $y_{\mathrm{jet}}/(b/2) = -0.6$, and a rectangular nozzle.

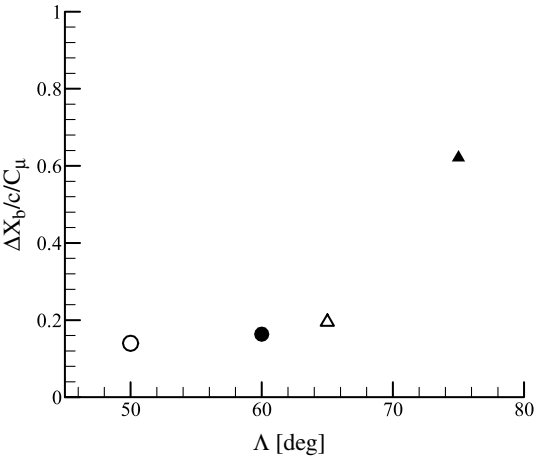

Fig. 13 Optimum effectiveness of a trailing-edge jet as a function of the wing sweep angle from various studies.

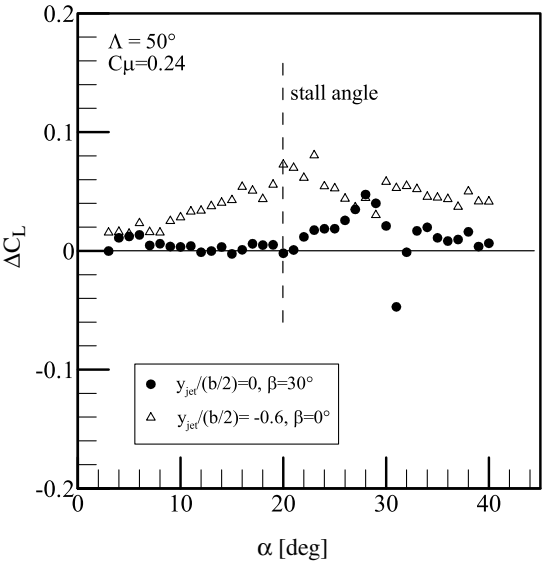

Fig. 14 Changes in lift coefficient for a nonslender wing with trailing-edge blowing with a circular nozzle.

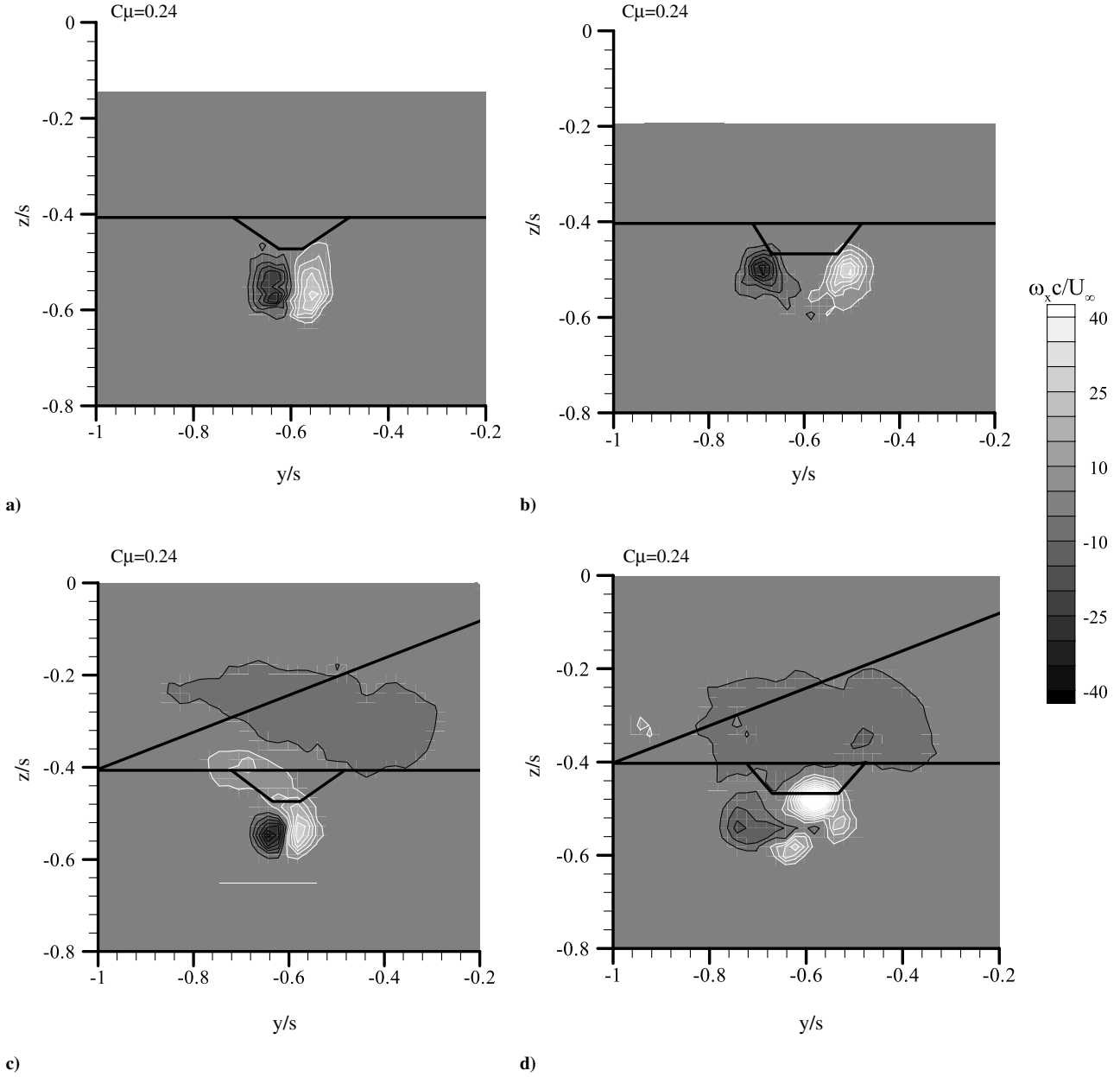

Fig. 15 Vorticity in a crossflow plane at $\Delta x/c = 0.25$ for a circular nozzle (left column) and rectangular nozzle (right column) with $\alpha = 20$ deg and $\beta = 0$ deg: a–b) jet only with no wing and c–d) with a nonslender wing.

to note that for highly yawed jets in crossflow, similar observations [18] were made. Only one sign of vorticity becomes dominant for the highly yawed jets, and the magnitude of the maximum vorticity is much larger than that of the vortices for the case of zero yaw. Even the two regions of concentrated vorticity (with the same sign) were observed in [18]. All of these features are similar to our observations.

Figure 16 shows a similar comparison for a larger angle of attack of $\alpha = 24$ deg in the poststall region. In this case, the wing vortical flow is even more disorganized and appears as weak vorticity patches above the nozzle. Nevertheless, the results are similar to those for $\alpha = 20$ deg. Distortion of the jet vortices is visible for the circular nozzle, with the counterclockwise jet vortex becoming elongated. The shape of the deformed jet vortex is entirely different for the rectangular nozzle. Although the counterclockwise vortex is not split into two as in the previous case ($\alpha = 20$ deg), there is strong similarity between the two cases. Again, the clockwise jet vortex is weak and there might be merging with the wing vortical flow, although this is not clear.

Figure 17 shows the effect of increasing momentum coefficient for the rectangular nozzle for $\alpha = 20$ deg. It is seen that vortex merging takes place for the larger momentum coefficient. The wing vortex (even though it is weak at the stall angle) merges with the clockwise jet vortex. We found evidence of the vortex merging for the slender wing as well. In this case, the wing vortex is expected to be more concentrated (compare Figs. 4 and 10). Figure 18 shows flow visualization pictures in a crossflow plane in the near wake ($\Delta x/c = 0.25$) for $\Lambda = 65$ deg and $\alpha = 10$ deg. The left column shows images when only the jet is marked, and the right column shows corresponding images when both the jet and vortex are marked with different color dyes. Flow visualization images are shown as a function of increasing jet pitch angle β. In all cases, the wing vortex appears to merge with the jet fluid on the left side (where the clockwise jet vortex is expected to be). As the jet pitch angle increases, the distortion of the jet and generation of the jet vortices are clear. Also, with increasing jet pitch angle, the jet vortices move away from the trailing edge and downward and, at the same time, the wing vortex becomes stretched.

Returning to the discussion of vorticity fields in Figs. 15 and 16, the jet–vortex interaction is much stronger for the rectangular nozzle. This is partly due to the larger separation distance of the vortex pair for the rectangular nozzle. Correspondingly, vortex-induced velocity over a larger distance generates a larger mass entrainment and even

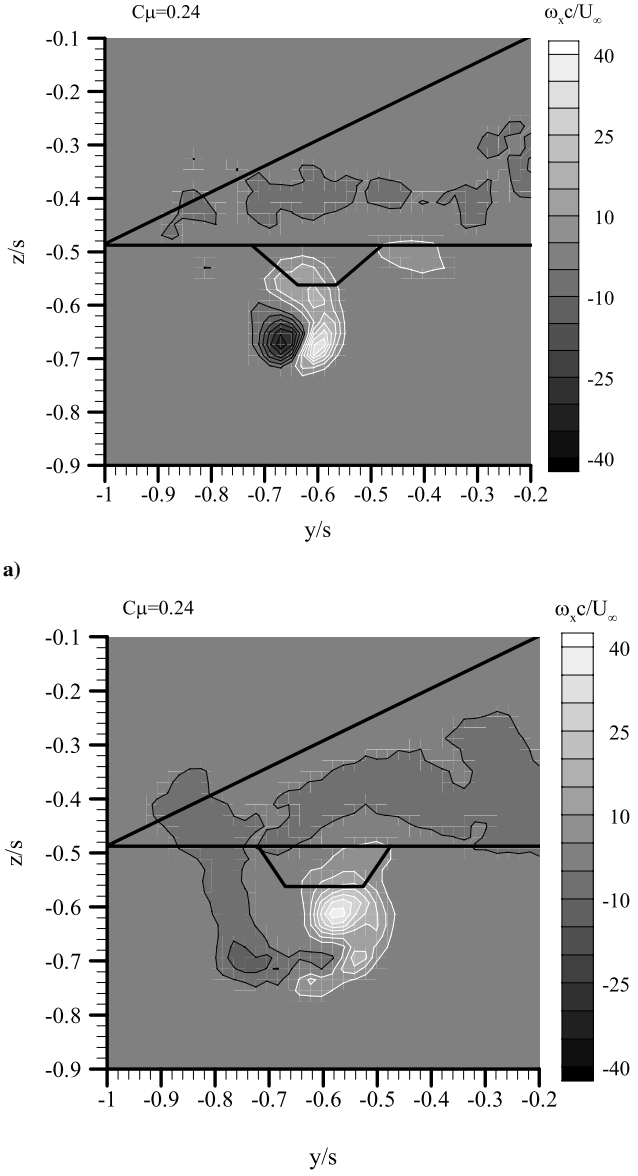

Fig. 16 Vorticity in a crossflow plane at $\Delta x/c = 0.25$ with $\alpha = 24$ deg and $\beta = 0$ deg: a) circular nozzle and b) rectangular nozzle.

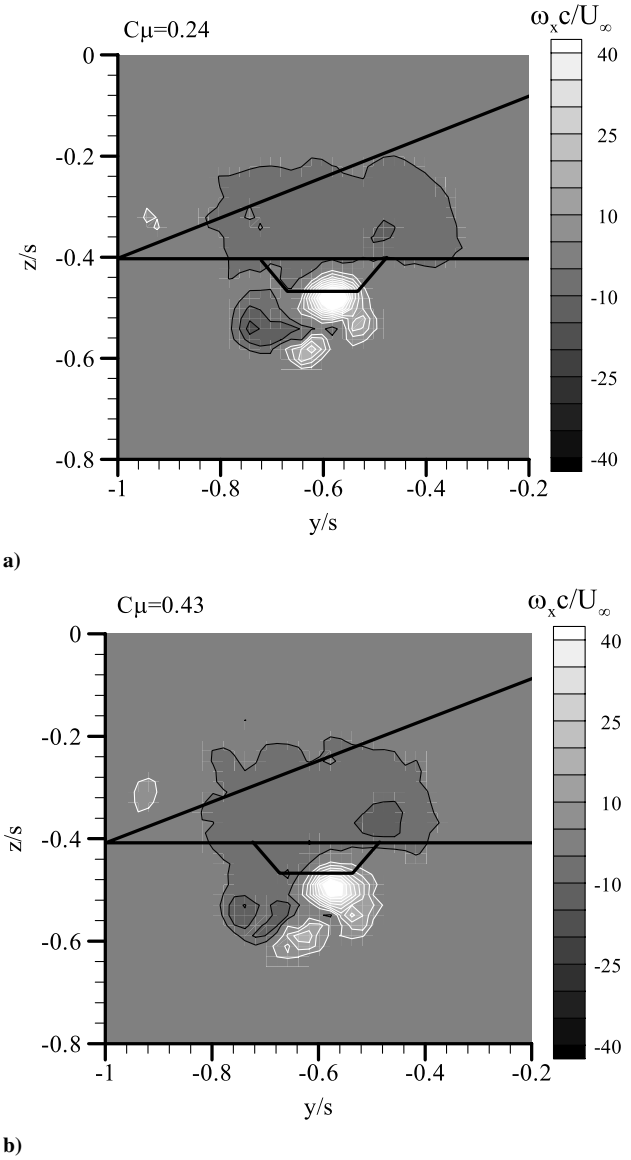

Fig. 17 Vorticity in a crossflow plane at $\Delta x/c = 0.25$ for a rectangular nozzle with $\alpha = 20$ deg and $\beta = 0$ deg.

pulls the leading-edge vortex downward. Wang et al. [21] showed that wing vortices may be drawn toward the jet center by the induced velocity created by the jet vortices. As a result, the rectangular nozzle has a larger influence on the delta wing aerodynamics, as evidenced by the force measurements shown in Fig. 14.

D. Effect of Jet Yaw Angle

Figure 19 presents the effect of the jet yaw angle γ on changes in C_L for the nonslender wing ($\Lambda = 50$ deg) and the slender wing ($\Lambda = 65$ deg) for $y_{\text{jet}}/(b/2) = -0.6$, $\beta = 0$, and $C_\mu = 0.24$. For the nonslender wing, as the jet yaw direction changed from outboard ($\gamma = -30$ deg) to inboard ($\gamma = 30$ deg), the increment in the lift coefficient ΔC_L displayed similar trends, which is also similar to that of the no-yaw case ($\gamma = 0$ deg), in particular, for the prestall incidences. In the poststall region, there are some differences, but the overall trend is similar. For all values of γ, ΔC_L increases with α and reaches its maximum values near the wing stall angle of $\alpha = 20$ deg.

In contrast with this observation, jet yaw angle has an entirely different effect on the aerodynamics associated with the slender wing. Figure 19b demonstrates that the outboard and inboard blowing produce different trends of lift increment. For outboard yaw ($\gamma = -30$ deg), ΔC_L appears to increase gradually with increasing α, which persists even after the stall angle of $\alpha = 32$ deg. When the jet is yawed inboard ($\gamma = 30$ deg), however, the changes in C_L are quite different from those associated with $\gamma = -30$ and 0 deg. The maximum ΔC_L (≈ 0.18) can be observed at a small wing incidence, that is, $\alpha = 3$ deg (Fig. 19b). As the wing incidence increases, ΔC_L keeps decreasing and reaches about zero near the stall angle. The substantial effect of yaw angle is a result of a relatively smaller span. Also, the relative contribution of vortical flows for the slender wing is larger. Unlike for nonslender wings, vortex lift makes up a large proportion of the total lift for slender wings.

To better understand why the slender wing is so sensitive to jet yaw angle, both small incidences and near-stall incidences were examined in detail. Flow visualization pictures for $\gamma = -30$, 0, and 30 deg are shown in Fig. 20 for the stall angle of $\alpha = 32$ deg. It is seen that vortex breakdown is delayed most for $\gamma = -30$, followed by $\gamma = 0$ and 30 deg. This is the same order as for the observed lift increment, shown in Fig. 19b.

For the case of small incidences, we conducted flow visualization and PIV measurements for $\alpha = 10$ deg, and the force increments were very different for $\gamma = 0$ and 30 deg. Flow visualization (not shown here) revealed that there is no breakdown at this incidence

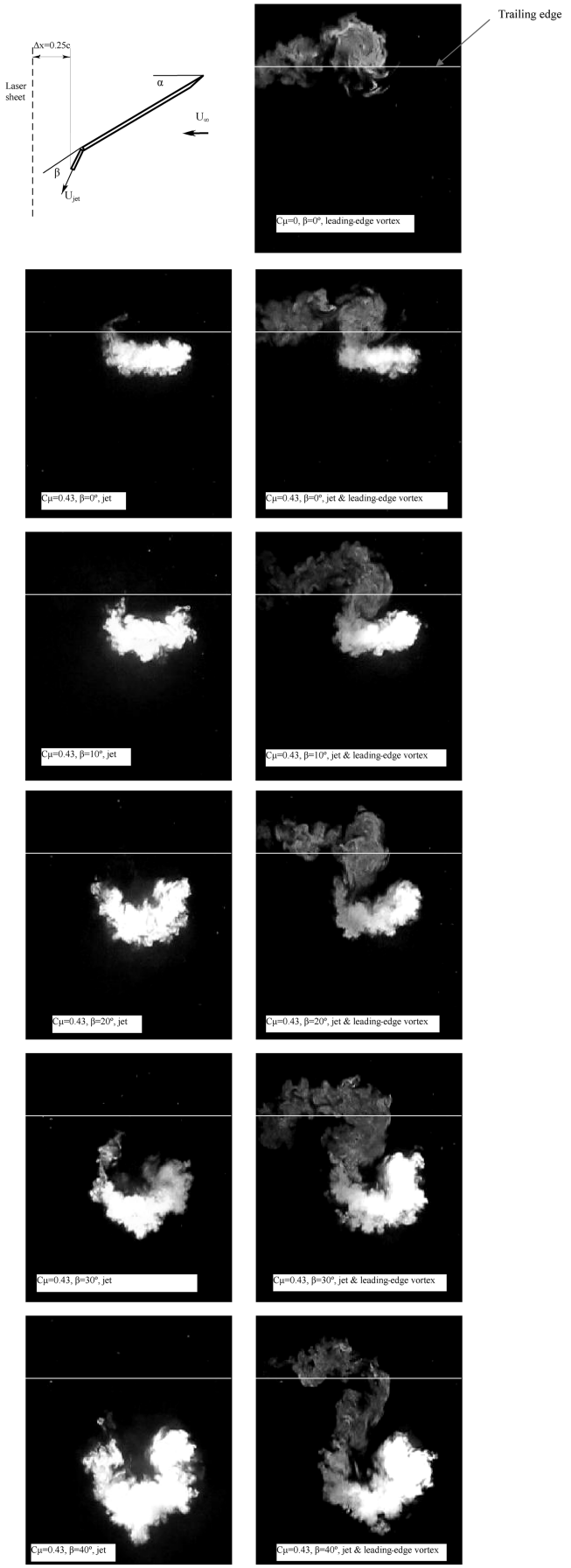

Fig. 18 Laser-fluorescence flow visualization in a crossflow plane at $\Delta x/c = 0.25$ with $\Lambda = 65\,\text{deg}$, $\alpha = 10\,\text{deg}$, $y_{\text{jet}}/(b/2) = -0.6$, and a rectangular nozzle.

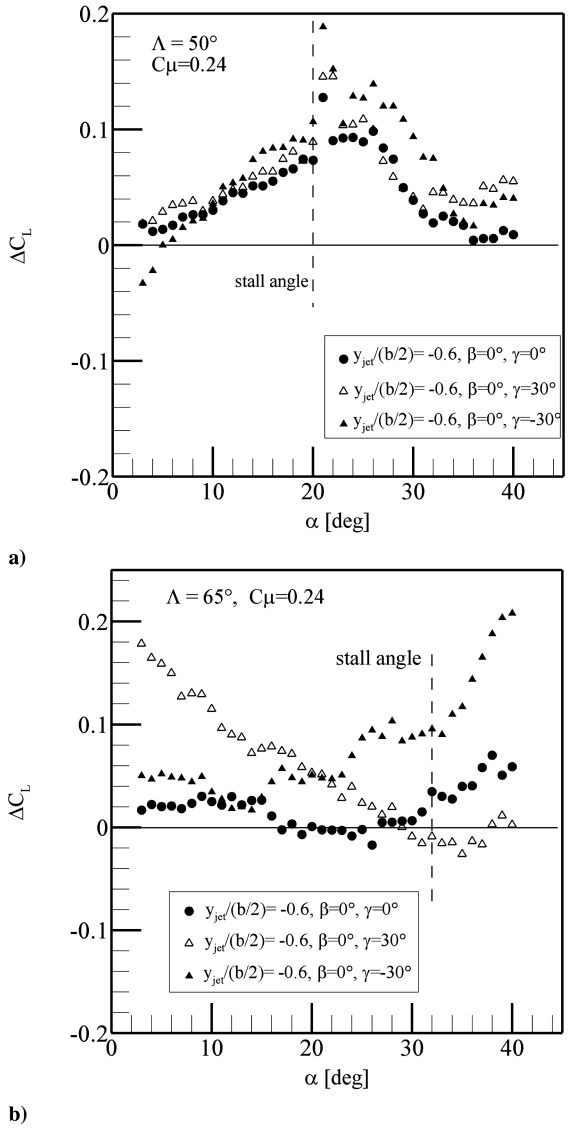

Fig. 19 Effect of the jet yaw angle on changes in C_L with $y_{\text{jet}}/(b/2) = -0.6$ and a rectangular nozzle: a) nonslender wing and b) slender wing.

regardless of the jet yaw angle. PIV measurements of the time-averaged vorticity in a crossflow plane at $x/c = 1.0$ are shown in Fig. 21 for these two values of yaw angle. Both the location of the leading-edge vortex and its structure are almost the same. The strength of the vortex was found as $\Gamma/U_\infty c = 0.147$ and 0.152 for $\gamma = 0$ and 30 deg, respectively. Velocity profiles (not shown here) also appeared very similar. It is concluded that the observed differences in the lift coefficient for the two jet yaw angles cannot be explained with any changes in the vortical flow properties. Because this implies that observed changes in the lift force are not related to the vortex lift, we suggest that the potential lift contribution might be responsible. Further studies are needed to understand the yaw sensitivity of slender wings at small incidences.

IV. Conclusions

The interaction of statically pitched trailing-edge jets with leading-edge vortices over stationary delta wings and its effects on the wing aerodynamics were investigated. For the nonslender wing ($\Lambda = 50\,\text{deg}$), the effect of the jet strongly depends on the spanwise location of the nozzle. For centerline blowing [$y_{\text{jet}}/(b/2) = 0$], the effect is small, whereas for undervortex blowing, the maximum lift enhancement reaches $\Delta C_{L,\max} \approx 0.15$ near the stall angle of $\alpha = 20\,\text{deg}$. The effect of the jet pitch angle β is relatively small. Flow visualization confirmed that the largest effect of blowing is

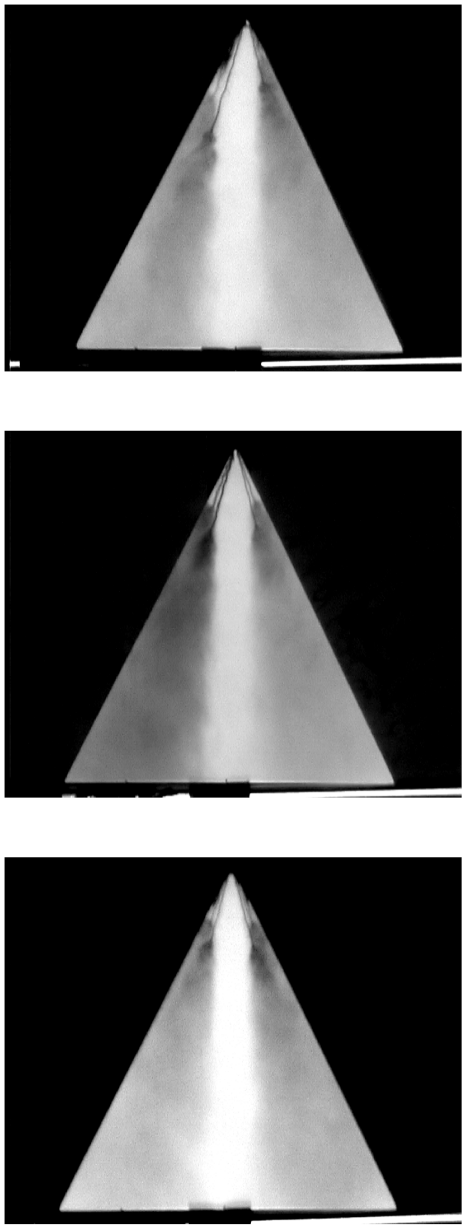

Fig. 20 Flow visualization for three different values of the jet yaw angle with $\alpha = 32\,\text{deg}$, $\Lambda = 65\,\text{deg}$, and $C_\mu = 0.24$.

observed near the stall incidence and poststall region, in which earlier reattachment of the shear layer occurs and vortex breakdown is delayed. PIV measurements at the stall angle of $\alpha = 20\,\text{deg}$ also confirmed the earlier reattachment and delay of vortex breakdown.

For the slender wing, the effect of trailing-edge blowing on the lift force is generally similar, with the lift force increasing substantially with the undervortex blowing near the stall angle and in the poststall region. However, the effect of the centerline blowing is relatively larger, due to the relatively shorter span of the wing. Flow visualization confirmed that the effect of blowing on the reattachment and breakdown location is small at low incidences and largest effects appear near the stall and in the poststall region. The jet pitch angle β has a relatively small effect on vortex breakdown, which is consistent with the force measurements. Delay of vortex breakdown with blowing is somewhat larger for the slender wing ($\Lambda = 65\,\text{deg}$), and there is evidence that the effectiveness of trailing-edge blowing increases with the wing sweep angle.

Force measurements revealed that the effect of nozzle geometry can be important, because the entrainment effect of the jet depends on it. PIV measurements showed that wing vortical flow interacts with the jet-induced vortices in the near wake. Large distortion of the jet

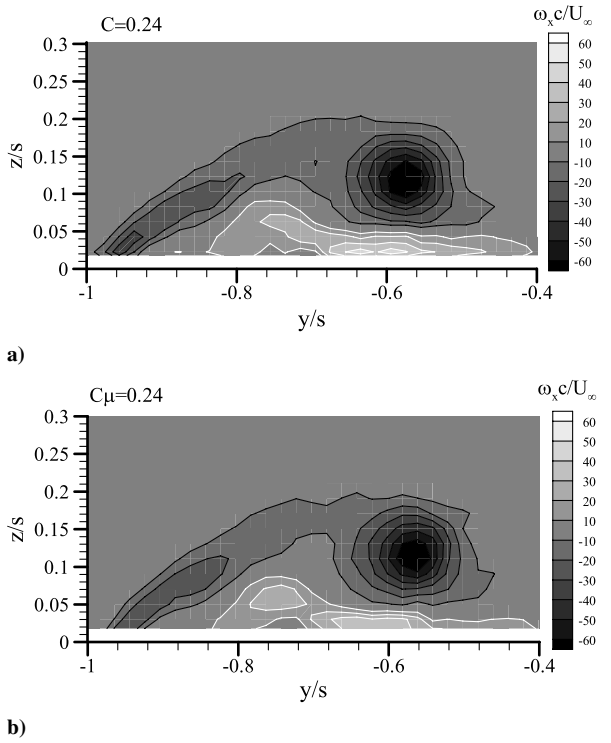

Fig. 21 Time-averaged crossflow vorticity field at the trailing edge ($x/c = 1.0$) with $\Lambda = 65\,\text{deg}$, $\alpha = 10\,\text{deg}$, $\beta = 0\,\text{deg}$, $y_{\text{jet}}/(b/2) = -0.6$, and a rectangular nozzle: a) $\gamma = 0\,\text{deg}$ and b) $\gamma = 30\,\text{deg}$ (inboard blowing).

vortices and formation of multiple vortices in some cases are revealed from these measurements. The merging of wing vortices with jet vortices is also observed. Overall, the jet–vortex interaction is much stronger for the rectangular nozzle and has a larger influence on the delta wing aerodynamics.

The effect of the jet yaw angle is small for the nonslender wing ($\Lambda = 50\,\text{deg}$), whereas the aerodynamics of the slender wing ($\Lambda = 65\,\text{deg}$) is very sensitive to the jet yaw angle. Near the stall angle, this sensitivity is due to the effect on vortex breakdown and vortex lift, which makes up a large proportion of the total lift for slender wings. On the other hand, at small incidences, no noticeable effect was found on the vortical flow and the observed changes in the forces might be due to the potential lift contribution.

Ongoing work includes unsteady aspects of dynamic thrust vectoring and jet/vortex interaction. Hysteresis and large phase lags associated with the wing vortical flows are expected to be important for dynamically pitching/yawing jets and maneuvering wings.

Acknowledgments

This work is jointly funded by the Engineering and Physical Sciences Research Council (EPSRC) and the Ministry of Defence, as well as by the EPSRC Academic Fellowship in Unmanned Air Vehicles.

References

[1] Earnshaw, P. B., and Lawford, J. A., "Low-Speed Wind-Tunnel Experiments on a Series of Sharp-Edged Delta Wings," Aeronautical Research Council, Reports and Memoranda No. 3424, 1964.

[2] Wentz, W. H., Jr., and Kohlman, D. L., "Vortex Breakdown on Slender Sharp-Edged Wings," *Journal of Aircraft*, Vol. 8, No. 3, 1971, pp. 156–161.

[3] Lee, M., and Ho, C. M., "Lift Force of Delta Wings," *Applied Mechanics Reviews*, Vol. 43, No. 9, 1990, pp. 209–221.

[4] Gursul, I., "Recent Developments in Delta Wing Aerodynamics," *The Aeronautical Journal*, Sept. 2004, pp. 437–452.

[5] Gursul, I., "Vortex Flows on UAVs: Issues and Challenges," *The Aeronautical Journal*, Dec. 2004, pp. 597–610.

[6] Gursul, I., "Review of Unsteady Vortex Flows over Slender Delta Wings," *Journal of Aircraft*, Vol. 42, No. 2, Mar.–Apr. 2005, pp. 299–319.

[7] Werle, H., "Quelques Resultants Experimentaux sur les Ailes en Fleche, aux Faibles Vitesses, Obtenus en Tunnel Hydrodynamique," *Recherche Aéronautique*, Vol. 41, Sept.–Oct. 1954.

[8] Lambourne, N. C., and Bryer, D. W., "The Bursting of Leading Edge Vortices: Some Observation and Discussion of the Phenomenon," Aeronautical Research Council, Reports and Memoranda No. 3282, 1962.

[9] Helin, H. E., and Watry, C. W., "Effects of Trailing-Edge Jet Entrainment on Delta Wing Vortices," *AIAA Journal*, Vol. 32, No. 4, 1994, pp. 802–804.

[10] Shih, C., and Ding, Z., "Trailing-Edge Jet Control of Leading-Edge Vortices of a Delta Wing," *AIAA Journal*, Vol. 34, No. 7, 1996, pp. 1447–1457.

[11] Vorobieff, P. V., and Rockwell, D. O., "Vortex Breakdown on Pitching Delta Wing: Control by Intermittent Trailing-Edge Blowing," *AIAA Journal*, Vol. 36, No. 4, 1998, pp. 585–589.

[12] Mitchell, A. M., Barberis, D., Molton, P., and Delery, J., "Control of Leading-Edge Vortex Breakdown by Trailing Edge Injection," *Journal of Aircraft*, Vol. 39, No. 2, 2002, pp. 221–226.

[13] Phillips, S., Lambert, C., and Gursul, I., "Effect of a Trailing-Edge Jet on Fin Buffeting," *Journal of Aircraft*, Vol. 40, No. 3, 2003, pp. 590–599.

[14] Gursul, I., Gordnier, R., and Visbal, M., "Unsteady Aerodynamics of Nonslender Delta Wings," *Progress in Aerospace Sciences*, Vol. 41, No. 7, 2005, pp. 515–557.

[15] Wang, Z., and Gursul, I., "Effects of Jet/Vortex Interaction on Delta Wing Aerodynamics," *1st International Conference on Innovation and Integration in Aerospace Sciences*, Quenn's Univ. Belfast, Paper CEIAT 2005-0054, Aug. 2005.

[16] Yavuz, M. M., and Rockwell, D., "Control of Flow Structure on Delta Wing with Steady Trailing-Edge Blowing," *AIAA Journal*, Vol. 44, No. 3, Mar. 2006, pp. 493–501.

[17] Wang, F. Y., and Zaman, K. B. M. Q., "Aerodynamics of a Jet in the Vortex Wake of a Wing," *AIAA Journal*, Vol. 40, No. 3, 2002, pp. 401–407.

[18] Milanovic, I. M., and Zaman, K. B. M. Q., "Fluid Dynamics of Highly Pitched and Yawed Jets in Crossflow," *AIAA Journal*, Vol. 42, No. 5, May 2004, pp. 874–882.

[19] Zhang, X., "Turbulence Measurements of a Longitudinal Vortex Generated by an Inclined Jet in a Turbulent Boundary Layer," *Journal of Fluids Engineering*, Vol. 120, 1998, pp. 765–771.

[20] Taylor, G., and Gursul, I., "Buffeting Flows over a Low-Sweep Delta Wing," *AIAA Journal*, Vol. 42, No. 9, Sept. 2004, pp. 1737–1745.

[21] Wang, F. Y., Proot, M. M. J., Charbonnier, J. M., and Sforza, P. M., "Near-Field Interaction of a Jet with Leading-Edge Vortices," *Journal of Aircraft*, Vol. 37, No. 5, 2000, pp. 779–785.